

Comprehensive Engineering Frequency Domain Analysis and Vibration Suppression of Aircraft Based on ADRC

Litao Liu^{1,2}, Bingwei Tian^{1*}

¹ Institute for Disaster Management and Reconstruction, Sichuan University, Chengdu, 610207, China

² Pittsburgh Institute, Sichuan University, Chengdu, 610207, China

* Corresponding authors: Bingwei Tian (bwtian@scu.edu.cn)

ABSTRACT

An aircraft was crashed almost vertical posture on 21 March 2022 in Wuzhou, Guangxi, China, which has created a strong debate in civil aviation industry. We proposed an active disturbance rejection controller (ADRC) for suppressing aircraft elastic vibration at the simulation level. ADRC, with relative simple structure, has been confirmed in several fields that its controlling effect is superior to classical proportion-integration-differentiation (PID) control theory, and it is easier to realize the transformation from theory to practice. In this article, the aircraft's vibration model is modeled based on the first elastic vibration mode of the aircraft. In addition, the principles of ADRC are illustrated in detail, a second-order ADRC is designed to control the elastic vibration model and the closed-loop frequency domain characteristics, tracking effect, and sensitivity of the system are analyzed. The estimated error of the extended state observer (ESO) is analyzed and the anti-disturbance effect of the closed-loop system and the robustness is verified using the Monte Carlo method. The simulation result illustrates that ADRC has a good suppression effect on the elastic vibration of the aircraft, and the closed-loop system has strong robustness in the face of dynamic parameters.

Introduction

Civil aviation companies have tendency to adopt aircraft designs with larger aspect ratios to reducing their induced drag for achieving speed breakthroughs and reducing fuel consumption in recent years. However, this design sacrifices the stability of the vehicle and leads the aircraft to vibrate during flight¹. Compared to conventional designs, slender vehicles have greater wave resistance and are subject to increased reaction forces. Therefore, more obvious and continuous vibration will occur with the improvement of civil aircrafts^{1,2}. Corresponding to the fatigue theory of engineering mechanics, elastic vibrations in flexible aircraft reduce their service life and may even damage the mechanical structure at certain specific frequencies, leading more serious effects³.

In recent years, scholars have been focusing on how to efficiently suppress the elastic vibrations of aircraft to enhance their performance. Chatter suppression techniques can be divided into two major categories, namely passive suppression, and active suppression. Passive chatter suppression mainly seeks more stable operation at the expense of vehicle performance, such as increasing airframe weight and reducing flight distance⁴. Active suppression is mainly for effectively suppress the flutter phenomenon by optimizing the control system of the aircraft. Active Flutter Suppression (AFS) technique can be traced back to the research content of the famous project—Active Flexible Wing (AFW) in the late 20th century⁵. At present, the more mainstream active flutter suppression techniques include classical PID control, linear quadratic Gaussian (LQG) control, sliding mode (SM) control, fuzzy logic controller (FLC), etc. Fig. 1 shows the development of some active flutter suppression technologies in chronological order.

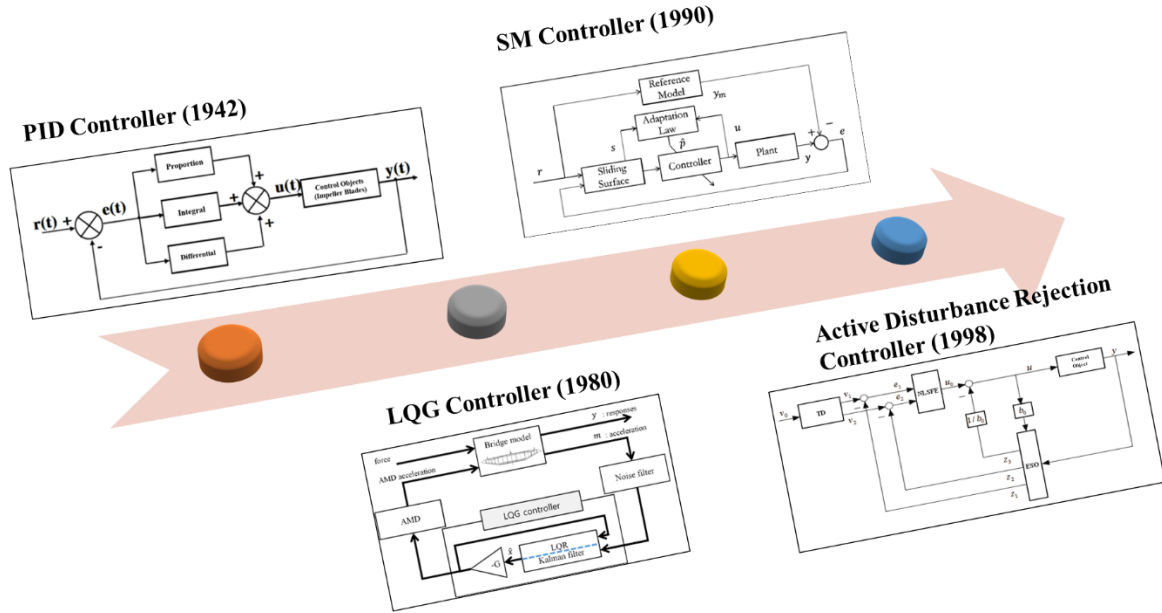


Figure 1. Development timeline of mainstream active flutter suppression controllers.

The invention of the PID control algorithm is mainly attributed to Ziegler and Nichols, who coined PID to the world in 1942⁶. PID is currently the most widely used control algorithm and govern the controller design subject. About 70 years later, Wang et al. developed a vibration model of the aircraft takeoff and the landing process to promote the performance of the landing gear system by PID control⁷. After nearly a century of development, the functions of PID have been over-explored to the extent that it is difficult to make a breakthrough. In recent years, quite a few scholars have tried to combine PID with different parameter-seeking models to improve the control effect⁸⁻¹⁰.

Gupta proposed LQG control for the first time and compared it with a conventional controller in 1980¹¹. In the three decades since then, scholars have tried to combine LQG with different feedback control strategies^{12,13}. In 2007, Na et al. applied the LQG control method was first used for a supersonic elastic system, and its usefulness in suppressing the amplitude and eliminating the observed spillover was revealed by numerical simulations¹⁴. A decade later, Franciszek realized the limitation of LQG in addressing with nonlinear problems, so he combined the H_∞ method with LQG to give a theoretical solution for nonlinear aeroelastic vibration¹⁵.

The sliding model was first proposed in 1990 and first used in aero control at the beginning of the 21st century¹⁶. In the 30 years since then, scholars have improved SMC strategies with different compensation methods to achieve higher accuracy in postures control and vibration suppression^{17,18}. In recent years, deep learning has brought epic changes to various fields. In 2020, Han et al. proposed a controller combining SMC and reinforcement learning to achieve greater robustness and control accuracy¹⁹. The SMC controller is robust and insensitive to parameter changes, and its development proposes solutions for uncertainty, making it possible to dispense with fault detection and isolation mechanisms²⁰.

However, researchers realized that the aforementioned algorithms have many problems, such as the PID algorithm seems to be too simple to adapt to the industry development; LQG, SMC, and other advanced algorithms have valid assumptions, but the mathematical form is too complex and requires high level controller design that is difficult to achieve a breakthrough from simulation to application. Therefore, many scholars are committed to seeking innovation and breakthroughs through other data processing methods. Among them, the capability of neural networks and deep learning provide us with possible solutions²¹⁻²³.

ADRC algorithm, as an innovative product of PID theory, is highly expected by developers to achieve the breakthrough from theory to practical application of advanced algorithms. ADRC was formally proposed by

Jingqing Han in 1998. The core of ADRC is the extended state observer (ESO) which estimates the states of systems, and subsequently compensates for the disturbance using the control law, making the controlled object change to a purely integral object²⁴. Han pointed out the problems of PID algorithms and solved the dilemma that PID was taking breakthroughs for decades²⁴⁻²⁶. Gao simplified Han's work and obtained the linear active disturbance rejection control (LADRC) technique, which makes parameters adjustment easier²⁷.

Regarding vehicle vibration suppression, the control effectiveness of ADRC has been affirmed by researchers at the simulation level. Liu et al. combined electromechanical actuator (EMA) with LADRC to propose a dynamic servo system and verified the effectiveness of the strategy through simulation and experiment²⁸. Yang et al. modeled a high aspect ratio UAV that used ADRC to suppress the elastic vibration of the fuselage, and the simulation results proved the improvement of the UAV performance²⁹. Chen and Zhao proposed an SVM-ADRC control strategy for UAVs to suppress the system chattering, and the simulation results demonstrated that SVM-ADRC is more robust than the standard ADRC³⁰. Wang et al. proposed an improved ADRC strategy to simulate and analyze the hypersonic vehicle model. By comparing the simulation results, it was verified that the novel strategy is more efficient³¹. Duan et al. modeled the helicopter load system to investigate the effect of load sway on the helicopter and confirmed the effectiveness of ADRC by comparing the results of ADRC and PID control³². Wang et al. analyzed the limit cycle oscillation suppression in the hovering state and obtained the conclude that ADRC performs better in suppressing limit cycle oscillation and eliminating attitude control errors by comparing it with the control results of the state feedback controller³³.

ADRC has already been applied in certain fields, such as finance³⁴ and industry³⁵, which has progressed to certain degrees due to the application of ADRC. For instance, in 2010, ADRC was used for the first time in a factory, which made a 41% reduction in energy consumption³⁵. Therefore, the role of ADRC algorithms in the aircraft controller design field is also highly anticipated and has a high research value.

On March 21, 2022, the near-vertical crash of China Eastern Airlines MU5735 aircraft becomes a hot topic around the world. This was China's most deadly crash in 28 years. There are air accidents every year in the global scale. Although the frequency of air accidents is not as frequent as traffic accidents is rare, however, the losses caused are tremendous. Behind every air crash, there seems to be a warning that the controllers need to reform to accommodate the needs of airlines and the needs of passengers. In this study, we primarily a comprehensive engineering frequency domain analysis of the aircraft elastic vibration model. The study further analyzes the closed-loop control effect by combining the established aircraft elastic vibration model with the designed second-order active disturbance rejection controller, the tracking performance and sensitivity of the closed-loop system are analyzed. Finally, the robustness of the system is verified by Monte Carlo shooting method.

Vibration model design

Maki *et al.* coined the vibration general model of aircraft in 1972³⁶, and Zhong *et al.* modeled the aircraft in 2021 based on the theory of Maki³⁷. A general mathematical model of pitch angle error of the aircraft and the first elastic mode is given by Eq. (1)³⁸.

$$\begin{cases} \ddot{\theta}(t) = -b_1\dot{\theta}(t) + b_2(\theta(t) + \alpha) - b_3u(t) - b_{11}\dot{q}_1(t) - b_{21}q_1(t) + d_1(t), \\ \ddot{q}_1(t) = -2\xi\omega_1\dot{q}_1(t) - \omega_1^2q_1(t) + c_1\dot{\theta}(t) + c_2\theta(t) + c_3u(t) - d_2(t), \end{cases} \quad (1)$$

where $\theta(t)$ is the difference between the angle at time t and the initial angle, $u(t)$ is the control signal, $q_1(t)$ is the first generalized elastic coordinate, ξ and ω_1 are the damping ratio and the natural frequency of the elastic mode respectively, c_3 represents the control gain of the elastic mode $q_1(t)$, c_1 , c_2 , b_{11} and b_{21} are the coupling coefficients between the pitch angle and the first mode, α is the angle of attack, $d_1(t)$ and $d_2(t)$ simulate the external disturbances to the system.

The transfer matrix (2) of the dynamical system (zero initial condition) is obtained. It is worth noting that the study of this section is only focused on the control object itself, so external disturbances $d_1(t)$ and $d_2(t)$ are temporarily ignored in this section and the angle of attack $\alpha = 0$ is assumed.

$$\begin{cases} \left(\frac{s^2 + b_1 s - b_2}{-b_3} \right) \Theta(s) + \left(\frac{b_{11} s + b_{21}}{-b_3} \right) Q(s) = U(s), \\ \left(\frac{-c_1 s - c_2}{c_3} \right) \Theta(s) + \left(\frac{s^2 + 2\xi\omega_n s + \omega_n^2}{c_3} \right) Q(s) = U(s). \end{cases} \quad (2)$$

According to Gramer's Law, the transfer function matrix (3) is calculated.

$$\begin{aligned} G_p &= \begin{bmatrix} G_1 \\ G_2 \end{bmatrix} = \begin{bmatrix} \frac{\Theta(s)}{U(s)} \\ \frac{Q(s)}{U(s)} \end{bmatrix} \\ &= \begin{bmatrix} \frac{(s^2 + 2\xi\omega_1 s + \omega_1^2)(-b_3) - (b_{11} s + b_{21})(c_3)}{\Delta(s)} \\ \frac{(c_1 s + c_2)(-b_3) + (s^2 + b_1 s - b_2)(c_3)}{\Delta(s)} \end{bmatrix}, \end{aligned} \quad (3)$$

where,

$$\begin{aligned} \Delta(s) &= s^4 + (2\xi\omega_1 + b_1)s^3 + (\omega_1^2 + 2\xi\omega_1 b_1 - b_2 + c_1 b_{11})s^2 + \\ &\quad (b_1 \omega_1^2 - 2\xi\omega_1 b_2 + c_2 b_{11} + c_1 b_{21})s + c_2 b_{21} - b_2 \omega_1^2. \end{aligned} \quad (4)$$

$b_1 = 0.05, b_2 = 4, b_{11} = 0.0005, b_{21} = 0.05, c_1 = 0.05, c_2 = 30, \xi = 0.006, \omega_1 = 30 \text{ rad/s}, b_3 = 13$ and $c_3 = 330$ ³⁷. Get the Bode plots of the dynamic system, as shown in Fig. 2.

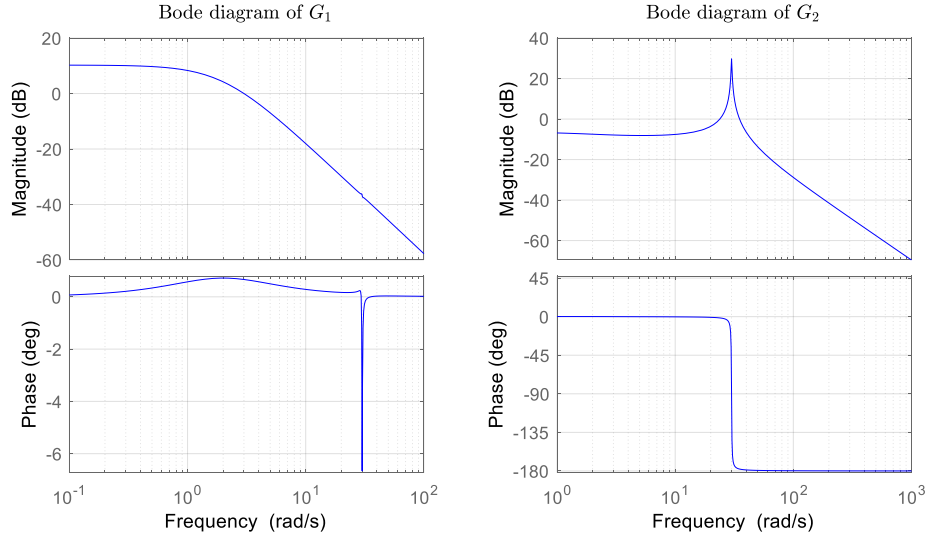


Figure 2. The Bode plots of G_1 and G_2 .

For the transfer function G_1 with a bandwidth (w) of $w_1 = 1.28 \text{ rad/s}$, the resonant peak (Mr) and resonant frequency (Rf) are $Mr_1 = 3.26 \text{ dB}$, $Rf_1 = 0 \text{ rad/s}$ respectively, and for the transfer function G_2 , w_2 equals to 43.38 rad/s , $Mr_2 = 30.60 \text{ dB}$, and $Rf_2 = 30.00 \text{ rad/s}$ (equals to ω_1). In general, the system bandwidth is relatively large, which means that the system has a strong tracking ability to step signal. The resonance peak and resonance frequency are relatively large, which means that the system has low stability when responding to step signals.

Active disturbance rejection controller design

The ADRC control system mainly consists of two parts—extended state observer (ESO) and proportion-differentiation (PD) control law. In this section, we design a second-order ADRC from these two parts, summarize how to simplify ADRC parameter adjustment, and analyze the closed-loop system and its sensitivity.

Extended state observer

For any dynamic system, it could be represented by Eq. (5).

$$y^{(n)} + a_1 y^{(n-1)} + \dots + a_{n-1} y^{(1)} + a_n y = k(u^{(m)} + b_1 u^{(m-1)} + \dots + b_{m-1} u^{(1)} + b_m u) + w, \quad (5)$$

where $y^{(n)}$ refers to the n th order derivative of the control object output, $u^{(m)}$ refers to the m th order derivative of the control signal, w is unknown for all external disturbances, and the coefficient vectors \vec{a} and \vec{b} where any element $\in \mathbb{R}$. The general expression for \ddot{y} is obtained by

$$\ddot{y} = f + b_0 u. \quad (6)$$

Consider $a_{n-2} = 1$, $b_0 \approx b_m$, f contains all the terms in Eq. (5) except $y^{(2)}$ and u ; thus, f is expressed by

$$f(y^{(n)}, y^{(n-1)}, \dots, u^{(m)}, \dots, u^{(1)}, w), \quad (7)$$

where f is defined as the generalized disturbance, which includes all perturbations inside and outside the system. f is estimated by ESO to obtain \hat{f} , and design a control law (Eq. (8)),

$$u = \frac{-\hat{f} + u_0}{b_0}. \quad (8)$$

Rewrite Eq. (6),

$$\ddot{y} = (f - \hat{f}) + u_0, \quad (9)$$

where $(f - \hat{f})$ is the estimation error, and Eq. (6) can be rewritten as the state-space Eq. (10).

$$\begin{cases} \dot{x} = Ax + Bu + Ef, \\ y = Cx, \end{cases} \quad (10)$$

where

$$\begin{cases} \dot{x} = [\dot{x}_1 & \dot{x}_2 & \dot{x}_3]^T = [\dot{y} & \ddot{y} & \dot{\hat{f}}]^T, \\ A = \begin{bmatrix} 0 & 1 & 0 \\ 0 & 0 & 1 \\ 0 & 0 & 0 \end{bmatrix}, B = \begin{bmatrix} 0 \\ b_0 \\ 0 \end{bmatrix}, E = \begin{bmatrix} 0 \\ 0 \\ 1 \end{bmatrix}, \\ C = [1 \quad 0 \quad 0]. \end{cases} \quad (11)$$

ESO is used to estimate x_1 , x_2 and f . The estimated state-space equations are shown in Eq. (12).

$$\begin{cases} \dot{\hat{x}} = A\hat{x} + Bu + E\dot{\hat{f}} + L(x_1 - \hat{x}_1), \\ \hat{x}_1 = C\hat{x}, \end{cases} \quad (12)$$

where $\hat{x} = [\hat{y} \quad \hat{\dot{y}} \quad \hat{f}]^T$, $L(x_1 - \hat{x}_1)$ is estimated compensation items, L is expressed by $[\alpha_1 \quad \alpha_2 \quad \alpha_3]^T$, is the gain vector of ESO, and directly affects the performance of the observer. Rewriting Eq. (12) yields that

$$\dot{\hat{x}} = (A - LC)\hat{x} + Bu + E\dot{\hat{f}} + Lx_1. \quad (13)$$

The system could converge when the determinant of the matrix $(A - LC)$ is equal to zero.

$$\det(\lambda I - (A - LC)) = \det \begin{pmatrix} \lambda + \alpha_1 & -1 & 0 \\ \alpha_2 & \lambda & -1 \\ \alpha_3 & 0 & \lambda \end{pmatrix}. \quad (14)$$

The characteristic polynomial $p_{(n)}$ can be expressed as

$$p_{(n)} = \lambda^3 + \alpha_1 \lambda^2 + \alpha_2 \lambda + \alpha_3, \quad (15)$$

where $\alpha_1, \alpha_2, \alpha_3$ are the adjustable parameters. To simplify the work of parameter adjustment, the Eq. (16) is reasonable²⁷.

$$p_{(n)} = (\lambda + \omega_0)^3, \quad (16)$$

where $\alpha_1 = 3\omega_0, \alpha_2 = 3\omega_0^2$, and $\alpha_3 = \omega_0^3$.

PD control law

Assuming the estimate \hat{f} in Eq. (9) has good estimation, then we obtain

$$\ddot{y} = (f - \hat{f}) + u_0 \approx u_0, \quad (17)$$

and then solving for u_0 by classical PD control theory,

$$u_0 = k_p (r - \hat{x}_1) - k_d \dot{\hat{x}}_2. \quad (18)$$

Through Eqs. (17, 18) we can obtain the transfer function of the PD control law (19),

$$G_{pd} = \frac{k_p}{s^2 + k_d s + k_p}. \quad (19)$$

We also try to simplify the PD law's parameters²⁷, then

$$G_{pd} = \frac{k_p}{(s + \omega_c)^2}, \quad (20)$$

where $k_d = 2\omega_c$ and $k_p = \omega_c^2$, the final value theorem tells us that the pole occurs at $-\omega_c$, and if ω_c is greater than zero, the system will eventually stabilize³.

Closed-loop analysis

For the model of the aircraft in last section, it is proposed to use the second-order ADRC controller described above for its control. To simulate the real data capture mode during flight, it is assumed that there is a certain relationship Eq. (21) between the first mode $q_1(t)$ and the pitch angle error $\theta(t)$ ³⁷,

$$\theta_m(t) = \theta(t) + 0.2q_1(t), \quad (21)$$

where $\theta_m(t)$ is the state value acquired directly by the aircraft observer and 0.2 is the measured factor.

Combine the ESO with the dynamics model. Rewriting the state-space Eq. (10) obtains

$$\begin{cases} \dot{x} = \bar{A}x + \bar{B}u(t) + \bar{C}\dot{f}, \\ y = \bar{D}x. \end{cases} \quad (22)$$

where

$$\begin{cases} x = [\theta_m(t) \quad \dot{\theta}_m(t) \quad f]^T, \\ f = -b_1\dot{\theta}_m(t) + b_2(\theta_m(t) + \alpha) \\ \quad - b_{11}\dot{q}_1(t) - b_{21}q_1(t) + d_1(t), \\ \bar{A} = A, \\ \bar{B} = [0 \quad b_0 \quad 0]^T, \\ \bar{C} = [0 \quad 0 \quad 1]^T, \\ y = \theta_m(t), \\ \bar{D} = [1 \quad 0 \quad 0]^T. \end{cases} \quad (23)$$

ESO estimates the state vector x and obtains the estimating Eq. (24),

$$\hat{\dot{x}} = \bar{A}\hat{x} + \bar{B}u(t) + \bar{C}\hat{\dot{f}} + L(\theta_m(t) - \hat{\theta}_m(t)), \quad (24)$$

where

$$\begin{cases} \hat{x} = \begin{bmatrix} \hat{\theta}_m(t) & \dot{\hat{\theta}}_m(t) & \hat{f} \end{bmatrix}^T, \\ L = \begin{bmatrix} 3\omega_o & 3\omega_o^2 & \omega_o^3 \end{bmatrix}. \end{cases} \quad (25)$$

To obtain the control signal $u(t)$, it can be obtained by solving Eq. (18) for $u_o(t)$, and then converts to $u(t)$ from Eq. (8). Simplify the progress, gain that

$$u(t) = \frac{-\hat{f} + 2\omega_c(r - \hat{\theta}_m(t)) - \omega_c^2 \hat{\theta}_m(t)}{b_0}. \quad (26)$$

The aircraft model and the ADRC controller are successfully combined to form feedback closed-loop (see Fig. 3). Where G_p represents the controlled object and G_c and F together represent the active disturbance rejection controller (ADRC).

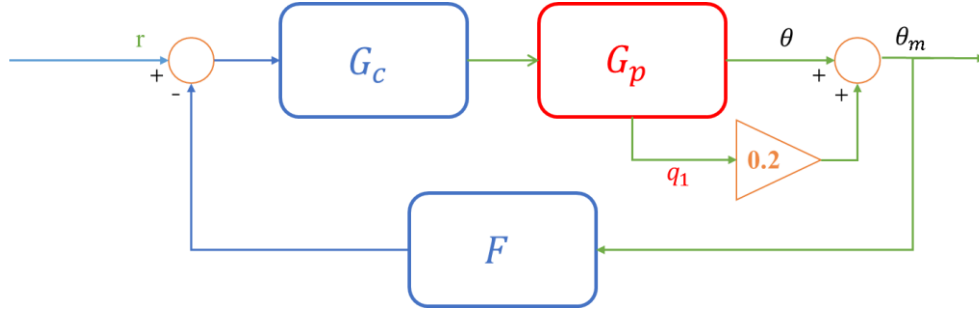


Figure 3. Closed-loop control system³⁸.

The transfer functions of the closed-loop system need to be analyzed to predict the system characteristics. The transfer function of ADRC that we design can be given by³⁸

$$\begin{cases} G_c = \frac{k_p(s^3 + \beta_1 s^2 + \beta_2 s + \beta_3)}{b_0[s^3 + (\beta_1 + k_d)s^2 + (\beta_2 + s^2\beta_1 + k_p)s]}, \\ F = \frac{(k_p\beta_1 + k_d\beta_2 + \beta_3)s^2 + (k_p\beta_2 + k_d\beta_3)s + k_p\beta_3}{k_p(s^3 + \beta_1 s^2 + \beta_2 s + \beta_3)}. \end{cases} \quad (27)$$

The transfer function of the controlled object is given by Eq. (3), and combining it with Eq. (27), the closed-loop transfer function G_{cl} could be found that

$$G_{cl} = \begin{bmatrix} G_{cl1} \\ G_{cl2} \end{bmatrix} = \begin{bmatrix} \frac{G_c G_1}{1 + F G_c G_1} \\ \frac{0.2 G_c G_1}{1 + 0.2 F G_c G_1} \end{bmatrix}. \quad (28)$$

Parameter tuning

By simplifying the parameters, three parameters are finally left, namely, b_0 , ω_0 and ω_c . The designed ADRC is simulated with the model for closed-loop feedback control, and a unit step setting signal is used to train the value of the parameters of ADRC. The final controller parameters are $\omega_0 = 7.8$ rad/s, $\omega_c = 1.68$ rad/s and $b_0 = -12.6$ obtained from the simulation model.

Fig. 4 illustrates the results of tracking effect and the control signal. As in Fig. 4, the pitch angle error peaks at 1.2942 rad at 3.58 s with a maximum overshoot of 29.42%. The set value of 1% is taken as the upper and lower limits of the acceptable state, i.e., the system is considered to reach the set value when $\theta_m(t)$ is at

[0.99,1.01]. The earliest adjustment time of the dynamics system within the acceptable range is 8.65 s. Analyzing the control signal, the minimum signal is minus 0.22 rad at 1.00 s and the maximum signal is 0.43 rad at 3.34 s. Such a smooth control signal is appreciable. Overall, the designed ADRC controller achieves a good control effect by parameter tuning. The frequency-domain of the closed-loop transfer functions needs to be analyzed.

Analyzing the Bode diagrams (Fig. 5) of the closed-loop transfer Eq. (28), for the transfer function G_{cl1} , the amplitude margin (Gm) equals to 49.43 dB, the phase margin (Pm) accounts for 60.34° , the cutoff frequency (Cf) is 30.00 Hz, and for G_{cl2} , the $Gm = 28.08$ dB, the $Pm = -89.39^\circ$, and the $Cf = 19.04$ Hz. The closed-loop system has relative high cutoff frequencies, which reflects the system's better ability to cope with the dynamic responses. The high amplitude margins indicate that the closed-loop system is more inclusive and stable.

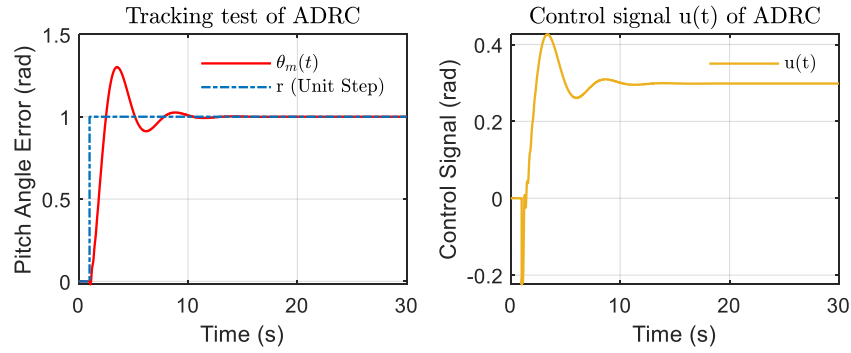


Figure 4. Control effect of ADRC on pitch angle of aircraft dynamics model under unit step signal (tracking test).

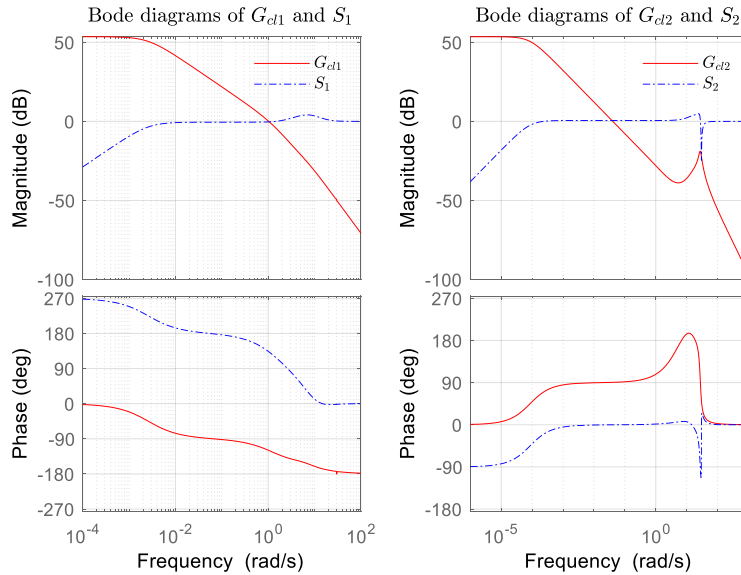


Figure 5. The Bode plots of G_{cl1} , G_{cl2} , S_1 and S_2 .

Closed-loop Sensitivity

Sensitivity is an important indicator of a closed-loop control system's robustness. For Eq. (28), the sensitivity function is given by³⁹

$$S = \frac{d \ln G_{cl}}{d \ln G_p} = \frac{d G_{cl}/G_{cl}}{d G_p/G_p} = \frac{G_p}{G_{cl}} \frac{d G_{cl}}{d G_p}. \quad (29)$$

Given that the parameters of the controller transfer function G_c are fixed and the parameters groups of the control object G_p is variable, bringing Eqs. (3, 28) into Eq. (29), and get via rewriting

$$S = \begin{bmatrix} S_1 \\ S_2 \end{bmatrix} = \begin{bmatrix} \frac{1}{1 + FG_c G_1} \\ \frac{1}{1 + 0.2FG_c G_2} \end{bmatrix}. \quad (30)$$

The Bode diagrams of S_1 and S_2 have been shown by the dotted lines (see Fig. 5). The Nyquist lines of $F(j\omega)G_c(j\omega)G_1(j\omega)$ and $0.2F(j\omega)G_c(j\omega)G_2(j\omega)$ are planned to draw in the imaginary coordinate system, and find the points where the distance from the graph line to the coordinate $(-1,0)$ is the smallest. The maximum sensitivity value can be obtained, and its significance is elaborated in Wang's book³⁹ where the maximum amplitude of the sensitivity M_s is given by

$$M_s = \max |S(j\omega)| = 1/r, \quad (31)$$

where r refers to the radius of inscribed circle whose center point is $(-1,0)$, it tangent to the Nyquist graph line in the imaginary coordinate system (see Fig. 6).

Fig. 6 is the sensitivity analysis results of the closed-loop system, the two inscribed circles radius r_1 and r_2 are 0.62 and 0.57, respectively. Thus, the maximum amplitude of the sensitivity M_{s1} and M_{s2} are 1.61 and 1.74. In fact, they are numerically equal to the resonant peak analyzed from the Bode diagrams. The maximum magnitude is less than 2 indicating the system is robust in the face of parameter changes⁴⁰.

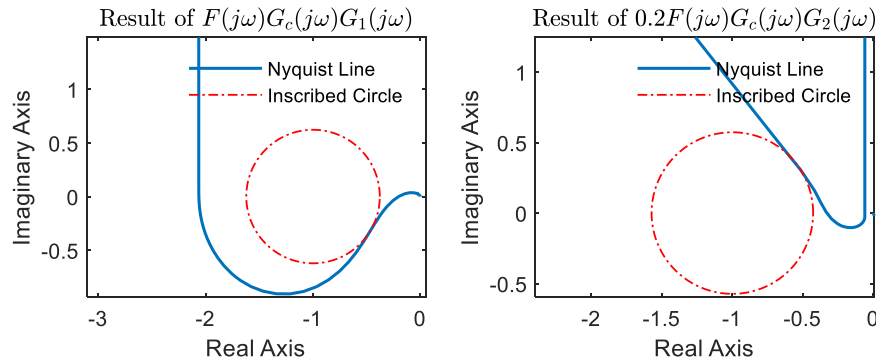


Figure 6. Sensitivity analysis results.

Simulation

In this section, the estimation error of ESO is discussed first, then the parameters of the aircraft model are randomly selected according to the Gaussian distribution. The simulation results of each group of parameters are analyzed and discussed robustness of the system. Fig. 7 illustrates the mathematical model used in the simulation, which is implemented by the Simulink of Matlab.

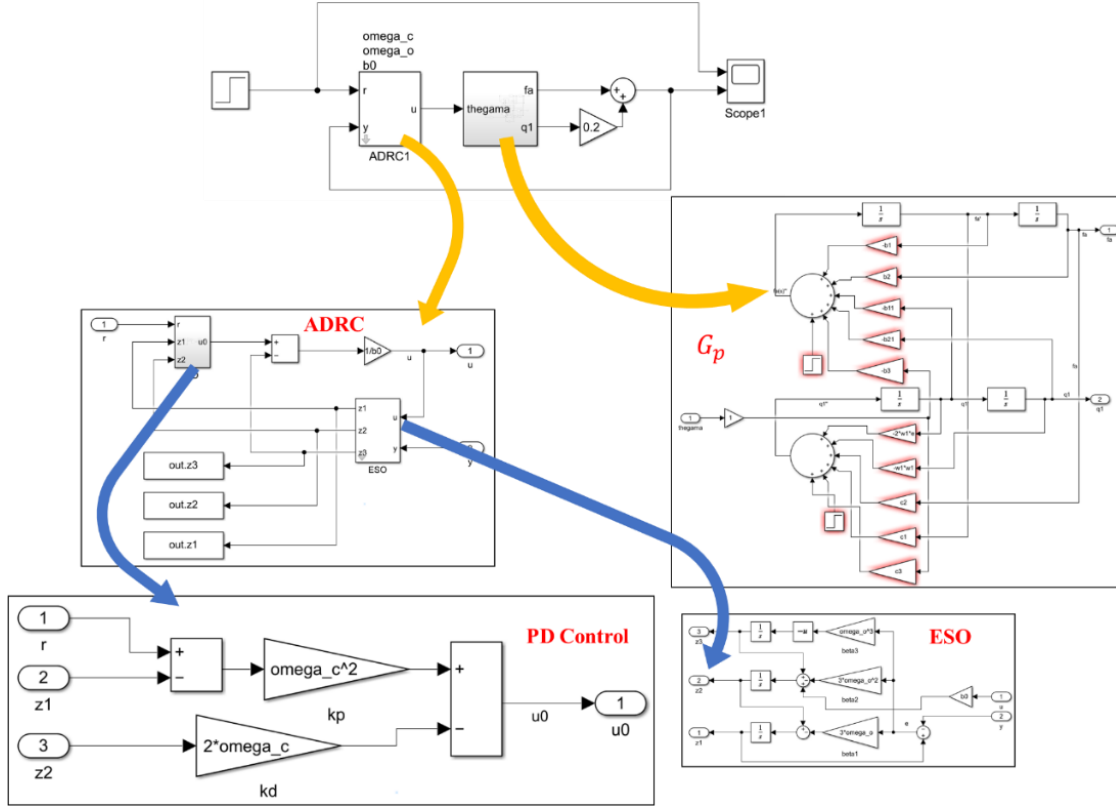


Figure 7. Simulation model building.

ESO estimation error analysis

One superiority of ADRC over the critical PD control law is its ability to make observed estimates of the states. The controlling effect of ADRC on pitch angle vibration suppression is closely related to the accuracy of the ESO estimates.

As shown in Fig. 8, the maximum estimation error of $\theta_m(t)$ occurs at 1.19 s with an error of 0.02 rad, and the estimation of $\theta_m(t)$ by ESO is very accurate. The maximum estimation error of $\dot{\theta}_m(t)$ occurs at 1.13 s with an estimation error of 0.64 rad/s. Overall, the ESO estimation of $\dot{\theta}_m(t)$ is relatively accurate. For the estimation of the total perturbation $f(t)$, the maximum estimation error is 14.78 rad/s², which occurs at 1.00 s. The effectiveness of ESO in estimating the total error seems to be less than satisfactory, but such a result is understandable due to its inclusion of total disturbances of the system that have more uncertainties. The estimation error for $f(t)$ stabilizes in the range of [-1,1] after 2.77 s and eventually becomes stable as the system converges. Overall, the ESO estimates of the state variables overlap to a large extent with the output response of the system, demonstrating the superiority of ADRC.

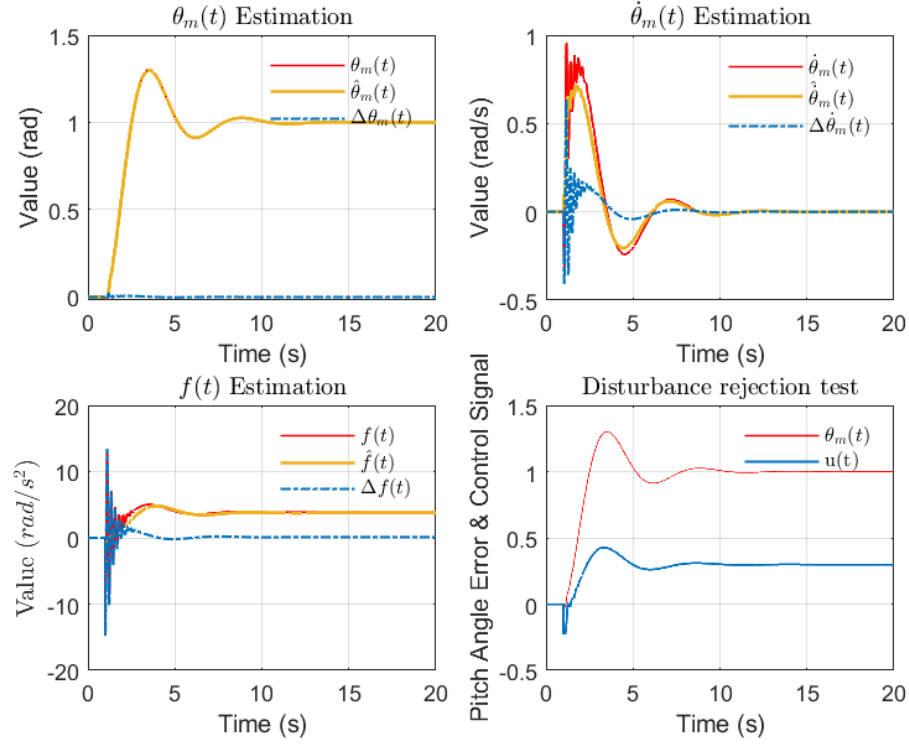


Figure 8. The estimated effects of ESO on states, and the disturbance rejection test.

Disturbance rejection test

The immunity of the system should be mentioned, and it is proposed to consider the step disturbance terms $d_1(t)$, $d_2(t)$ at 11 s, where $d_1(t) = 0.07 \text{ rad/s}^2$ and $d_2(t) = -1.00 \text{ m/s}^2$ ³⁷. The system responds to the disturbance terms after 15 s. The pitch angle maximum occurs at 18.56 s and is 1.0029 rad with a maximum overshoot percentage of 0.29%, which indicates that the system is always within the acceptable interval. At about 18s, the control signal $u(t)$ reaches the maximum value of 0.294 rad and finally converges to the control signal of 0.293 rad. The subtle changes in pitch angle and control signal prove that the system has relatively good immunity to disturbances.

Robustness analysis

In this part, an innovative ADRC robustness test method is designed, the main idea is based on Monte Carlo statistical analysis, using Gaussian distribution. It randomly takes values of parameters and randomly compose 12000 sets under the 3σ principle that guarantees 99.73% confidence level at the simulation level. The ranges of randomly taken values of each parameter are given by Eq. (32)³⁷. The median of each variable parameter is the mean value (μ) of the Gaussian distribution, and one-third of the difference between the mean and the upper or lower bound is used as the standard deviation (σ).

$$\begin{cases} \omega_1 = [24, 36] \text{ rad/s}, \\ b_2 = [3.2, 4.8], \\ b_3 = [10.4, 15.6], \\ c_3 = [264, 396], \\ d_1 = [-0.07, 0.07] \text{ rad/s}, \\ b_2 = [-1, 1] \text{ rad/s}^2. \end{cases} \quad (32)$$

Simulations perform for each set of parameters and the outputs are analyzed. Three indexes are planned to be selected to evaluate the system output, namely, setting time (the earliest moment when the controlled object stabilizes in the interval $[0.99, 1.01]$), maximum percentage overshoot (the percentage of maximum overshoot from the set value), and absolute error integral (the sum of the errors between the output value and the set value in the simulation time). Of the 12000 sets of data returned from the analysis, 248 sets had parameters that are outside the upper and lower bounds. Therefore, there are only 11,752 valid data sets.

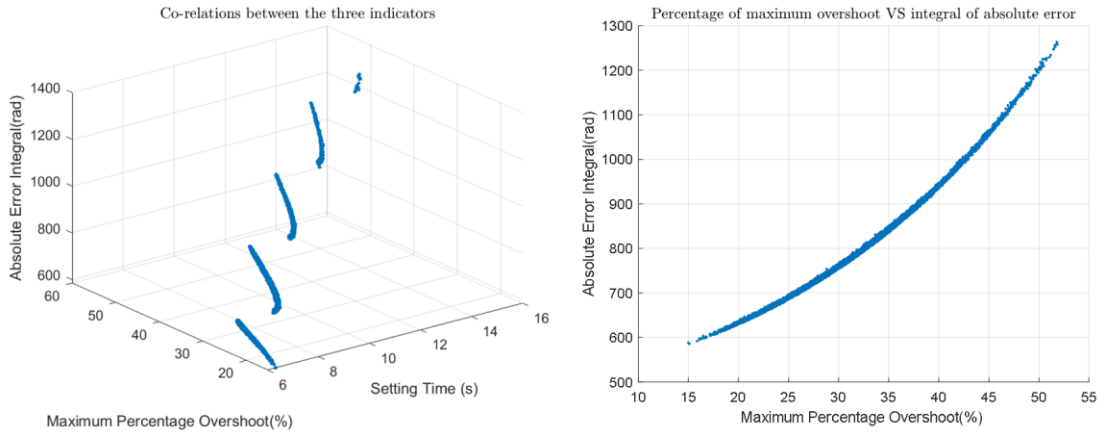


Figure 9. Monte Carlo shooting results.

Analyzing the data and Fig. 9, the setting time has a significant stratification phenomenon, which mainly occurs at 6.64 s, 8.92 s, and 11.32 s. The second stratification occurs at 8.92 s, and the data sets with the setting time of less than 8.92 s account for 80.62% of the total data sets. Moreover, the data sets with the maximum percentage overshoots less than 35% account for 76.65%. Absolute error integral is concentrated within 1200 rad, which has a strong linear relationship with the overshoot amount. Overall, the control system shows strong robustness in response to parameter changes.

Conclusion

The aircraft pitch angle vibration model was established and the system frequency domain characteristics were discussed comprehensively by a series of engineering analysis methods. A second-order ADRC was designed to control the model, while the closed-loop frequency domain characteristics and sensitivity were analyzed. The Monte Carlo shooting method was used to verify that the system presented excellent control effects in the face of large changes in system parameters. The structure of ADRC is relatively simple, which makes up for the shortcomings of the classical PID algorithm. It has the possibility of developing from simulation to practical application in the field of aerospace controller design, providing a possible solution for reducing the number of air accidents and adapting to the demands.

It is undeniable that the current model has certain limitations. The constant vibration frequency is the biggest deficiency of this research for in the actual flight mission and the vibration frequency is variable due to the unknown external and internal disturbances. Therefore, it is proposed to consider a deep learning algorithm such as critical recurrent neural networks (RNN) or long short-term memory neural networks (LSTM) in future research to monitor and predict the change of the system frequency at each moment, allowing ESO achieve more accurate disturbance prediction. However, the ADRC combined with the deep learning algorithm would lose its practicality to a certain extent.

References

1. Afonso, F., Coelho, M., Vale, J., Lau, F. & Suleman, A. On the Design of Aeroelastically Scaled Models of High Aspect-Ratio Wings. *Aerospace*. (2020).
2. Liu, J. , Lv, B. & Guo, H. Stiffness Experiment of Large Deformation and Large Aspect Ratio Elastic Wing Model. ICITEE2020: The 3rd International Conference on Information Technologies and Electrical Engineering. (2020).
3. Esfandiari, R. S. & Lu, B., Modeling and analysis of dynamic systems (CRC press, 2018).
4. Zhang C. W. & Cao L. Research on the development of aircraft active flutter suppression technology. Proceedings of the 12th Annual Conference on Control and Application of the Aviation Society of China (2006).
5. Nissim, E. & John J. Burken. Control surface spanwise placement in active flutter suppression systems. No. H-1492. (1988).
6. Ziegler, John G. & Nathaniel B. Nichols. Optimum settings for automatic controllers. *trans. ASME* 64.11 (1942).
7. Wang, H., Xing, J. T., Price, W. G. & Li, W. An investigation of an active landing gear system to reduce aircraft vibrations caused by landing impacts and runway excitations. *Journal of Sound and Vibration*. 317.1-2, 50-66 (2008).
8. Das, S., Anish A. & Indranil P. Simulation studies on the design of optimum PID controllers to suppress chaotic oscillations in a family of Lorenz-like multi-wing attractors. *Mathematics and Computers in Simulation*. 100, 72-87 (2014).
9. Bi, Y., Xie, C., An, C. & Yang, C. Gust load alleviation wind tunnel tests of a large-aspect-ratio flexible wing with piezoelectric control. *Chinese Journal of Aeronautics*. 30.1, 292-309 (2017).
10. Guo, B. T., Liu, H., Luo, Z & Wang, F. Adaptive PID controller based on BP neural network. 2009 International Joint Conference on Artificial Intelligence. IEEE (2009).
11. Gupta & Narendra K. Frequency-shaped cost functionals-Extension of linear-quadratic-Gaussian design methods. *Journal of Guidance and Control*. 3.6, 529-535 (1980).
12. Ahmad, S. M., Chipperfield, A. J. & Tokhi, O. Dynamic modeling and optimal control of a twin rotor MIMO system. Proceedings of the IEEE 2000 National Aerospace and Electronics Conference. NAECON 2000. Engineering Tomorrow (Cat. No. 00CH37093). IEEE, (2000).
13. Dong X. M., et al. Shock damping control of Mr stiffness and damping controllable buffer system. *Journal of Sichuan University: engineering Science Edition* 6 (2009).
14. Na, S. S., Librescu, L., Marzocca, P., Yoon, G. C., Rubillo, C. & Bong, K. Robust aeroelastic control of two-dimensional supersonic flapped wing systems. *Acta mechanica*. 192.1, 37-47 (2007).
15. Dul, F. Active suppression of freeplay aeroelastic vibrations of ailerons by robust control methods with incomplete measurements. *Aircraft Engineering and Aerospace Technology*. (2018).
16. Ye, J., Hu, Q. L. & Ma, G. F. Adaptive backstepping fault-tolerant control for flexible spacecraft with unknown bounded disturbances and actuator failures. *ISA transactions*. 49.1, 57-69 (2010).
17. Song, J. S., Choo, J., Cha, S. J., Na, S. & Qin, Z. Robust aeroelastic instability suppression of an advanced wing with model uncertainty in subsonic compressible flow field. *Aerospace Science and Technology*. 25.1, 242-252 (2013).
18. Zahra, R., Mohand, L. & Smain, D. Classical and fuzzy sliding mode control for a nonlinear aeroelastic system with unsteady aerodynamic model. *International Journal of Computing and Digital Systems*. 9.6, 1108-1099 (2020).

- ### Figure legends

Fig. 1 shows the development of some active flutter suppression technologies in chronological order.

14/16

For the transfer function G_1 with a bandwidth (w) of $w_1 = 1.28$ rad/s, the resonant peak (Mr) and resonant frequency (Rf) are $Mr_1 = 3.26$ dB, $Rf_1 = 0$ rad/s respectively, and for the transfer function G_2 , w_2 equals to 43.38 rad/s, Mr_2 is 30.60 dB, and Rf_2 is 30.00 rad/s (equals to ω_1). In general, the system bandwidth is relatively large, which means that the system has a strong tracking ability to step signal. The resonance peak and resonance frequency are relatively large, which means that the system has low stability when responding to step signals.

Figure 3. Closed-loop control system³⁸.

The aircraft model and the ADRC controller are successfully combined to form feedback closed-loop (see Fig. 3). Where G_p represents the controlled object and G_c and F together represent the active disturbance rejection controller (ADRC).

Figure 4. Control effect of ADRC on pitch angle of aircraft dynamics model under unit step signal (tracking test). Fig. 4 illustrates the results of tracking effect and the control signal. As in Fig. 4, the pitch angle error peaks at 1.2942 rad at 3.58 s with a maximum overshoot of 29.42%. The set value of 1% is taken as the upper and lower limits of the acceptable state, i.e., the system is considered to reach the set value when $\theta_m(t)$ is at [0.99,1.01]. The earliest adjustment time of the dynamics system within the acceptable range is 8.65 s. Analyzing the control signal, the minimum signal is minus 0.22 rad at 1.00 s and the maximum signal is 0.43 rad at 3.34 s. Such a smooth control signal is appreciable.

Figure 5. The Bode plots of G_{cl1} , G_{cl2} , S_1 and S_2 .

Analyzing the Bode diagrams (Fig. 5) of the closed-loop transfer Eq. (28), for the transfer function G_{cl1} , the amplitude margin (Gm) equals to 49.43 dB, the phase margin (Pm) accounts for 60.34°, the cutoff frequency (Cf) is 30.00 Hz, and for G_{cl2} , the $Gm = 28.08$ dB, the $Pm = -89.39^\circ$, and the $Cf = 19.04$ Hz. The closed-loop system has relative high cutoff frequencies, which reflects the system's better ability to cope with the dynamic responses. The high amplitude margins indicate that the closed-loop system is more inclusive and stable.

Figure 6. Sensitivity analysis results.

Fig. 6 is the sensitivity analysis results of the closed-loop system, the two inscribed circles radius r_1 and r_2 are 0.62 and 0.57, respectively. Thus, the maximum amplitude of the sensitivity Ms_1 and Ms_2 are 1.61 and 1.74. In fact, they are numerically equal to the resonant peak analyzed from the Bode diagrams. The maximum magnitude is less than 2 indicating the system is robust in the face of parameter changes⁴⁰.

Figure 7. Simulation model building.

Fig. 7 illustrates the mathematical model used in the simulation, which is implemented by the Simulink of matlab.

Figure 8. The estimated effects of ESO on states, and the disturbance rejection test.

As shown in Fig. 8, the maximum estimation error of $\theta_m(t)$ occurs at 1.19 s with an error of 0.02 rad, and the estimation of $\theta_m(t)$ by ESO is very accurate. The maximum estimation error of $\dot{\theta}_m(t)$ occurs at 1.13 s with an estimation error of 0.64 rad/s. Overall, the ESO estimation of $\dot{\theta}_m(t)$ is relatively accurate. For the estimation of the total perturbation $f(t)$, the maximum estimation error is 14.78 rad/s², which occurs at 1.00 s. The effectiveness of ESO in estimating the total error seems to be less than satisfactory, but such a result is understandable due to its inclusion of total disturbances of the system that have more uncertainties. The estimation error for $f(t)$ stabilizes in the range of [-1,1] after 2.77 s and eventually becomes stable as the system converges. Overall, the ESO estimates of the state variables overlap to a large extent with the output response of the system, demonstrating the superiority of ADRC.

Figure 9. Monte Carlo shooting results.

Analyzing the data and Fig. 9, the setting time has a significant stratification phenomenon, which mainly occurs at 6.64 s, 8.92 s, and 11.32 s. The second stratification occurs at 8.92 s, and the data sets with the setting time of less than 8.92 s account for 80.62% of the total data sets. Moreover, the data sets with the maximum percentage overshoots less than 35% account for 76.65%. Absolute error integral is concentrated within 1200 rad, which has a strong linear relationship with the overshoot amount. Overall, the control system shows strong robustness in response to parameter changes.

Acknowledgments

This work was supported by National Key Research and Development Program of China (2016YFC0802600) and the Fundamental Research Funds for the Central Universities (Sichuan University).

Author contributions

Programming, simulation, manuscript preparation and editing, and data analysis—Litao Liu, providing guidance, revision and finalization of manuscript—Bingwei Tian

Competing interests

The authors declare no competing interests.

Data availability

All data generated or analysed during this study are included in this published article and its supplementary information files.

Additional information

(Tentative)